Resolving the fundamentals of the *J*-integral concept by multi-method in situ nanoscale stress-strain mapping

Check for updates

Michael Meindlhumer [1,5] ✉, Markus Alfreider [1,5] ✉, Noel Sheshi [2], Anton Hohenwarter [1], Juraj Todt [1], Martin Rosenthal [3,4], Manfred Burghammer [3], Enrico Salvati [2], Jozef Keckes [1] & Daniel Kiener [1]

The integrity of structural materials is oftentimes defined by their resistance against catastrophic failure through dissipative plastic processes at the crack tip, commonly quantified by the *J*-integral concept. However, to date the experimental stress and strain fields necessary to quantify the *J*-integral associated with local crack propagation in its original integral form were inaccessible. Here, we present a multi-method nanoscale strain- and stress-mapping surrounding a growing crack tip in two identical miniaturized fracture specimens made from a nanocrystalline FeCrMnNiCo high-entropy alloy. The respective samples were tested in situ in a scanning electron microscope and a synchrotron X-ray nanodiffraction setup, with detailed analyzes of loading states during elastic loading, crack tip blunting and general yielding, corroborated by a detailed elastic-plastic finite element model. This complementary in situ methodology uniquely enabled a detailed quantification of the *J*-integral along different integration paths from experimental nanoscale stress and strain fields. We find that conventional linear-elastic and elastic-plastic models, typically used to interpret fracture phenomena, have limited applicability at micron to nanoscale distances from propagating cracks. This for the first time unravels a limit to the path-independence of the *J*-integral, which has significant implications in the development and assessment of modern damage-tolerant materials and microstructures.

Comprehending and quantifying fracture characteristics constitute pivotal steps in mitigating structural component failure and enhancing the longevity of modern materials in various applications. To quantitatively assess the fracture resistance of (brittle) materials, linear-elastic fracture mechanics (LEFM) was developed over 100 years ago[1,2]. It is based on thermodynamic considerations linking the energy released upon crack extension to the energy required for creation of new fracture surfaces. The resulting stress σ and strain ε solutions around the crack tip contain mathematical singularities originating from a $r^{-0.5}$ term, where r is the radial distance from the crack tip. LEFM deals with these singularities by focusing on the elastically loaded region outside the plastic zone (PZ) in the closest crack tip vicinity and scaling the $r^{-0.5}$ behaviour with so-called stress intensity factors K. LEFM and its extension to small-scale yielding are applicable when the elastic stress field around the crack tip[1], the so-called K-field, is dominant (in size) and crack tip plasticity is minimal. Consequently, it is restricted to brittle or semi-brittle materials

or specimen geometries of unwieldy size, up to meters for very ductile materials.

When small-scale yielding conditions are not met, elastic-plastic fracture mechanics concepts, such as the crack-tip opening displacement[3] and *J*-integral[4] are necessitated. While the first is a purely geometric concept, the latter is based on energetic considerations of an isotropic Ramberg-Osgood[5] type hardening material. Close to the crack tip, where the (e.g. von Mises) stress exceeds the material yield stress (hence, within the PZ), the stress and strain increase is linked to the *J*-integral, with a proportionality of $\sigma \propto r^{-1/n+1}$ and $\varepsilon \propto r^{-n/n+1}$, ($n$ being the Ramberg and Osgood hardening parameter[5]), analogous to K and $r^{-0.5}$ in LEFM. While this so-called HRR-theory (after Hutchinson[6], Rice and Rosengren[7]) also deals with singularities when reaching the crack tip and thus also neglects material decohesion, it is able to incorporate plastic deformation in front of the crack tip[6,7]. In linear-elastic materials[8] $J = K^2 \cdot \frac{1-\nu^2}{E}$, where E and ν are the elastic modulus and the Poisson's ratio, respectively. The accurate mathematical definition of *J* is

based on a positive contour integral around a 2D crack tip, which is path independent if specific simplified assumptions hold[4]. The subjects of integration include the non-linear strain energy density and the traction forces normal to the integration contour, which include the stress and strain field around the crack tip. Therefore, the only possibility to directly assess J as a function of varying contour paths[4] is *combined local strain and stress field mapping* in the crack tip vicinity.

There have been several attempts to measure the individual elastic, plastic and/or total strains and stresses in front of a crack tip. Synchrotron or neutron diffraction have been proven vital to evaluate the elastic strain contribution (transforming it directly into stress) in front of cyclically[9–15] and unidirectionally loaded[16–18] cracks. Recently, cross-sectional X-ray nanodiffraction (CSnanoXRD) has been employed to investigate the multiaxial stress fields of multilayers during and after severe deformation[19,20] or during crack growth[18], resolving not only the 2D stress tensor perpendicular to the incident focused X-ray beam, but also the size and shape of the plastic zone[18]. To quantify crack growth[21] and the total strain in front of the crack, tip digital image correlation (DIC) techniques are state-of-the-art[22]. Furthermore, X-ray diffraction-based elastic strain analysis and DIC total strain analysis were combined to explore stress and strain field evolution resulting from overload events during cyclic loading[12]. Another recent in situ method combines electron backscatter diffraction (EBSD) with strain tracking by DIC of a speckle pattern on the sample surface[23]. Though this approach provides superior total strain resolution by DIC in the scanning electron microscope (SEM) and adequate elastic strain resolution from the EBSD patterns, both at nearly the same volume depth, it is restricted to small deformation steps and single-crystalline or coarse-grained materials. In contrast, an in situ SEM-DIC based method proposed by Alfreider et al.[24] utilizes pre-milled point feature tracking for the determination of total strain on the sample surface while also considering large plastic deformations during a *continuous straining experiment*. Combined, these advancements let to this study's primary objective: the one-of-a-kind direct experimental evaluation of the J-integral during in situ loading of a fracture specimen. Such accomplishment uniquely enables the verification of established fracture mechanics concepts in a realistic experiment, their validity and boundary conditions, with all caveats and unexpected deformation characteristics that might occur in modern highly damage tolerant materials[25–28].

High entropy alloys[29] are increasingly investigated for their alleged chemical, thermal and mechanical stability[30,31], which may enable new sustainable materials design[32] based on promising mechanical properties of this new material class[33–35]. For example, a NbTaTiHf alloy exhibits superior room temperature fracture toughness by a dynamic competition of screw and edge dislocations at the crack tip[28], while multiplicity of dislocation pathways and negative mixing enthalpy promote high ductility in MoNbTi[26] and HfNbTiVAl$_{10}$[27], respectively. Especially the herein studied Cantor alloy (CoCrFeMnNi)[36] has drawn significant attention due to its enormous fracture toughness of ~270 MPa m$^{1/2}$ even at cryogenic temperatures[25], while it retains its ductility and high yield strength in nanocrystalline state[24,37]. This renders it a perfect material for the objective of this work, the validity assessment of local J-integral analysis via simultaneous investigation of the *local stress* (elastic deformation) and *strain state* (total deformation) *in front of a crack tip*. Additionally, the high yield stress σ_y of nanocrystalline materials renders them desirable for responsible device design[38,39], but synthesis of bulk nanocrystalline materials for conventional techniques and sample sizes is challenging. We overcome this challenge by utilizing micromechanical testing methods[40–45].

In this work, we conduct a thorough analysis of local stress and strain tensors by in situ CSnanoXRD (Fig. 1a) and in situ SEM-DIC (Fig. 1b) on two nearly identical microcantilevers with $(a/W)_{\text{CSnanoXxRD}} = 0.347 \pm 0.005$ and $(a/W)_{\text{SEM}} = 0.351 \pm 0.005$, respectively, while the bending lengths L was adapted to the differing widths B (5% difference between CSnanoXRD and SEM cantilevers) to apply a nominally equal stress intensity at the crack tip. The in situ SEM experiment involved continuous quasi-static deformation, while the in situ CSnanoXRD experiment was performed stepwise with an adapted bending length adjusting for

similar nominal K_I at the crack tip, guided by preceding SEM load-displacement data. Crack growth was monitored in SEM by sequential unloading, which was further used for standardized global calculation of the J-integral, while small-angle X-ray scattering (Fig. 1a, c)[46] and full width at half maximum (FWHM) microscopy[19] were utilized to track crack growth and microstructural changes during the CSnanoXRD experiment, respectively. Additionally, the experimental data were complemented by a 3D elastic-plastic finite element (FE) model. Combining experimental stress and strain data enabled to calculate the J-integral as a function of the contour distance from the crack tip in three fundamental load regimes: during elastic loading (LS1), crack tip blunting (LS2) and general yielding (LS3). This unprecedented combination of two in situ nanoscale approaches is employed for the first time to directly assess an experimental J-integral (J_{comb}) at the close crack tip vicinity, reflecting its original theoretic description[4]. The evaluation conducted with varying integration paths (Fig. 1b) indicates a strong path dependence of the J-integral within the plastically deformed region, in contrast to the original concept. Furthermore, it allowed novel insights into the defect dominated deformation and fracture behaviour of nanocrystalline high entropy alloys to guide future material design.

Results
Representative multi-method in situ data
Here only representative correlative in situ data will be presented from two near-identical cantilevers. Full details regarding mechanical tensile characteristics of the material as well as similarity of the experiments and implications on the here presented results will be given in Supplementary Notes 1 and 2, respectively.

Figure 2a, b depict the normal ε_{yy} and shear ε_{yz} strain at LS2 as representative strain components, respectively. The normal strain depicts a butterfly-shape region in front of the crack tip as described by classical fracture theories[1,6–8]. Furthermore, a transitional gradient from high tensile to high compressive stresses as a result from the bending geometry of the specimen is evident. The shear strains show slight stochasticity in the form of unphysical compression/tensile undulations. However, the antisymmetric trend for shear strains in front of a crack tip is evident[1,6–8]. Detailed strain components (ε_{yy}, ε_{zz}, ε_{yz}, and ε_{xx}) for all loadsteps in analogy to the CSnanoXRD data as well as the full videos compiled thereof are provided in Supplementary Note 3 (Supplementary Fig. S4 and Movies S1–S4).

Again, the acquired microstructure and stress data obtained at LS2 in the in situ CSnanoXRD experiment are shown in Fig. 2c–h, while CSnanoXRD maps for all individual loadsteps are fully detailed in Supplementary Note 4. The small-angle X-ray scattering microscopy (SAXSM) micrograph in Fig. 2c shows that the crack length increased to 11.4 ± 0.5 μm with clearly detectable crack tip blunting. The advantage of SAXSM against current electron microscopy-based crack length detection is that each pixel in the 2D plot is averaged over the cantilever thickness, providing a volumetric crack length average representative for the whole specimen rather than only a surface crack length.

The averaged FWHM map at LS2 in Fig. 2d shows an increase in the area up to ~8 μm in front of the crack tip, indicating defect accumulation (e.g. dislocation emission, stacking faults) due to plastic deformation originating from applying mechanical load on the crack tip. However, compared to LS1, the FWHM is decreased in the immediate crack tip vicinity (compare Supplementary Fig. S7 and Supplementary Note 4). Conversely, a decrease of the FWHM is evident in the highly compressive region at the lower part of the specimen. This indicates recombination/removal of mobile defects introduced through the high pressure torsion (HPT) process[47–49].

The σ_{yy}, σ_{zz}, and σ_{yz} stress distributions obtained at LS2 are presented in Fig. 2e–g, respectively. While the σ_{yy} stress distribution exhibits a superposition of the bending and crack tip stress fields (Fig. 2e), the σ_{zz} and σ_{yz} stress distributions are governed exclusively by the crack tip stress field (Fig. 2f, g, respectively), according to fracture mechanics theory[8].

$\sigma_{\text{von Mises}}(y, z)$ at LS2 (Fig. 2h) exhibits a typical butterfly-like stress distribution ahead of the crack tip. The maximum of $\sigma_{\text{von Mises}}(y, z)$ was

Fig. 1 | Schematic visualization of in situ synchrotron and in situ SEM experiments. Here, L, B, and W are the bending length, thickness and width of the cantilevers, respectively, while a is the crack length and BS indicates the beam stop (**a**). The cantilever deformed in SEM was continuously loaded, and a video recorded for tracking the spots to evaluate the total surface strains (**b**). Additionally, the elliptic lines in (**b**) show integration contours for J-integral evaluation, being small (8 μm), medium (16 μm) and wide (24 μm) ellipses at closest (1 μm) and maximum crack tip distance (13 μm) configurations, respectively. In (**c**) a detail of a SAXSM micrograph around the crack tip is shown with the coordinate system used to evaluate the relevant crack opening stress (COS) and growth direction stress (GDS) components parallel and perpendicular to the local crack tip coordinate system, respectively. The scale bars in (**b** and **c**) are 5 μm.
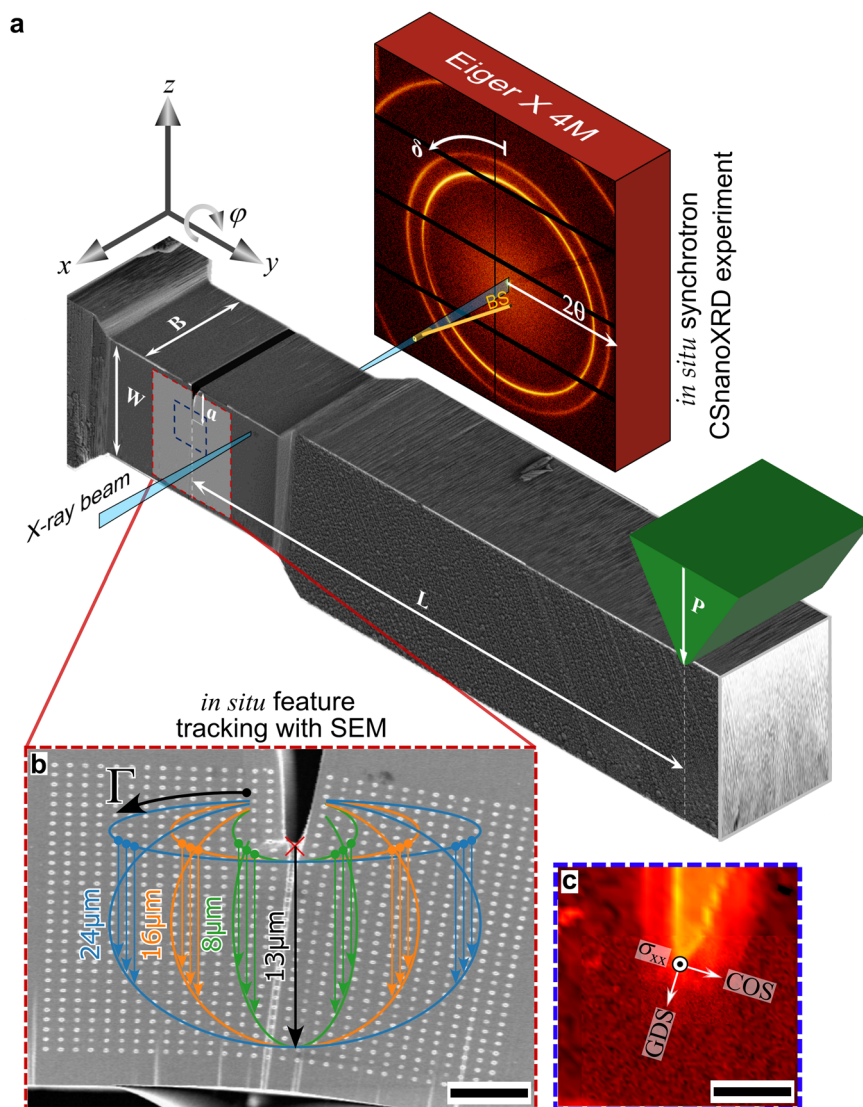
found to be ~2.04 GPa, close to the reported yield stress between ~2 GPa[37] and 2.35 GPa[24] for this specific nanocrystalline high entropy alloy (HEA). However, at LS2, the maximum $\sigma_{\text{von Mises}}(y, z)$ value of ~2.51 GPa was found at the lower cantilever half, where the stress state is close to uniaxial compression (cf. Fig. 2e–g). Analysis of $\sigma_{\text{von Mises}}(y, z)$ magnitudes thus indicates that the yield stress is reached both in front of the crack tip as well as at the bottom of the cantilever.

Individual deformation regimes

Figure 3 shows the equivalent crack tip strains in the highly deformed regions (±30–60 deg) gathered from the in situ SEM experiment for all loadsteps, while Fig. 4 sums up relevant characteristics for the three fundamental regimes: elastic loading (LS1, first column), transition to plastic deformation (LS2, second column) and general yielding (LS3, third column), respectively. Thereby, the first row depicts the stresses in front of the crack tip, the second row depicts maps of the plane-strain test plane strain test (PST) (cf. Methods) and the near crack tip region (green circle with a diameter of 5 μm) from which the respective PST distributions in the third row are taken. PST can be correlated with the Poisson's ratio $v = 0.253 \pm 0.017$[24] of the present material. The fourth row details individual maps of stress-triaxiality T. Again, full details of the CSnanoXRD stress characteristics are given in Supplementary Note 4. Additionally, FE modelling was performed to corroborate the experimental data and Fig. 5 shows the comparison between the

experimental and modelled $\sigma_{\text{von Mises}}$ distributions. Full details regarding the results from the FE model are given in Supplementary Note 5.

At LS1, Fig. 3 shows that the maximum crack tip strains rise to ~0.05, already beyond the elastic limit in tension experiments[24], suggesting finite plastic deformation at the crack tip. After a limited region with a $r^{-0.5}$ decrease, which suggests the transition to a linear elastic K-field, a considerably steeper decrease of the strain is evident at ~1.5 μm crack tip distance due to the bending gradient dominating the deformation.

The stress distributions are mainly controlled by the elastic (K-) field (Fig. 4a). Deviations occur very close to (<200 nm) and far from (>2.5 μm) the crack, indicating the presence of PZ and bending stress gradient, respectively. The PST ratio (Fig. 4d), used to determine the stress state (Eq. 2, Methods), increases slightly towards the notch and aligns well with reported Poisson's ratios of v_{exp} of 0.253 ± 0.017[24] and 0.25 ± 0.1[50] of the FeCrMn-NiCo HEA (Fig. 4g). This confirms that the cantilever is mostly under plane-strain conditions near the notch, conforming to elastic fracture mechanics theory[8].

Similar to the PST ratio, the stress triaxiality ratio T (Eq. 3) provides insight into the nature of the stress concentrations in front of the notch. Generally, a high tensile stress triaxiality favors crack growth by void formation and coalescence over plastic shear deformation, i.e. shear lip formation[8,51].
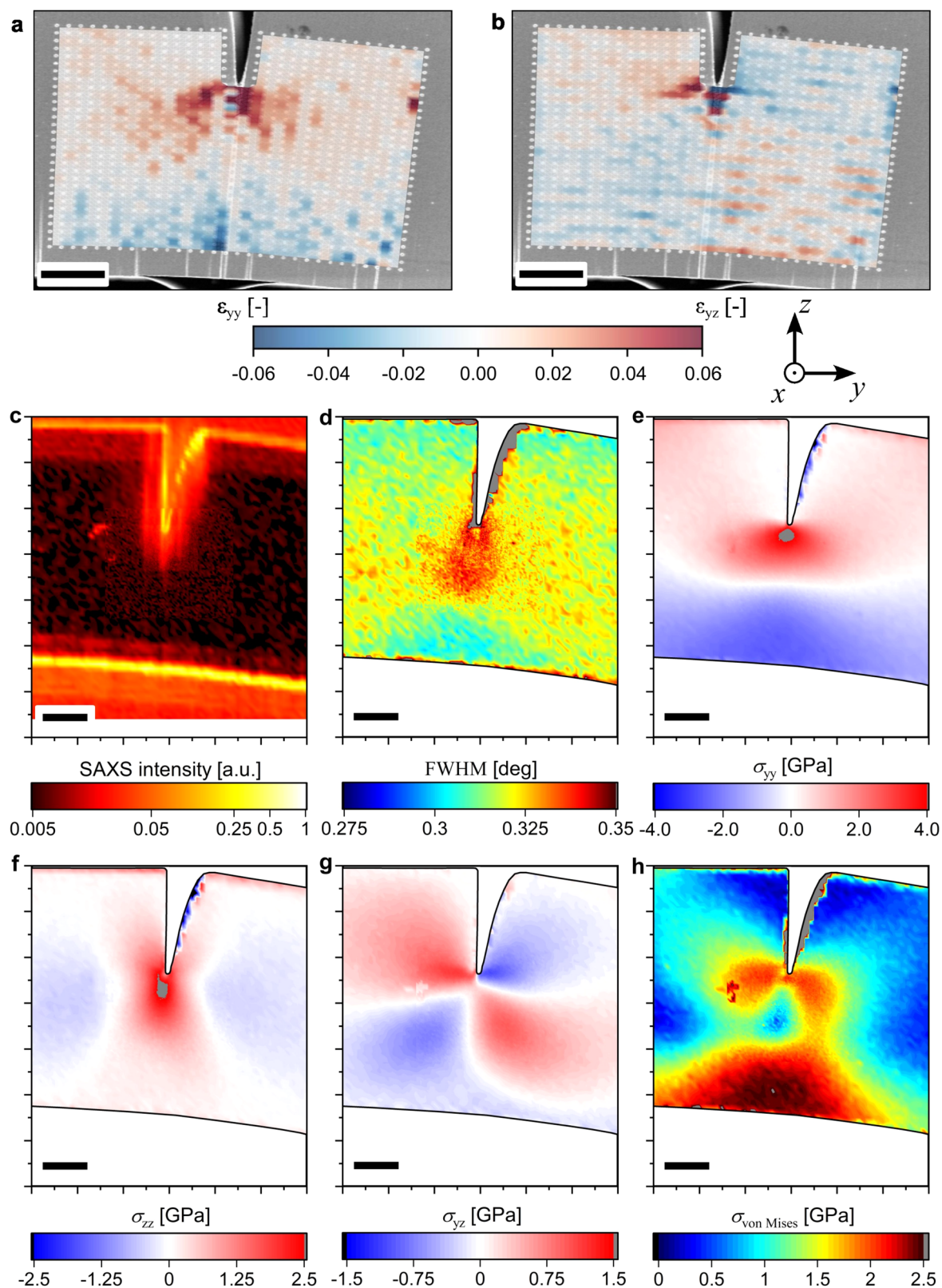
Fig. 2 | Representative in situ SEM and CSnanoXRD data at LS2. In situ SEM data (**a**, **b**) showing total normal ε_{yy}-strains and shear ε_{yz}-strains. The CSnanoXRD data (**c–h**) provides SAXS micrographs (**c**) used for quantitative crack growth evaluation, while average FWHM data (**d**) details qualitatively the microstructural evolution. Stress components σ_{yy}, σ_{zz}, and σ_{yz} are given in (**e–g**), while the $\sigma_{\text{von Mises}}$ distribution calculated from the respective stress components is shown in (**h**). All scale bars correspond to 5 μm.
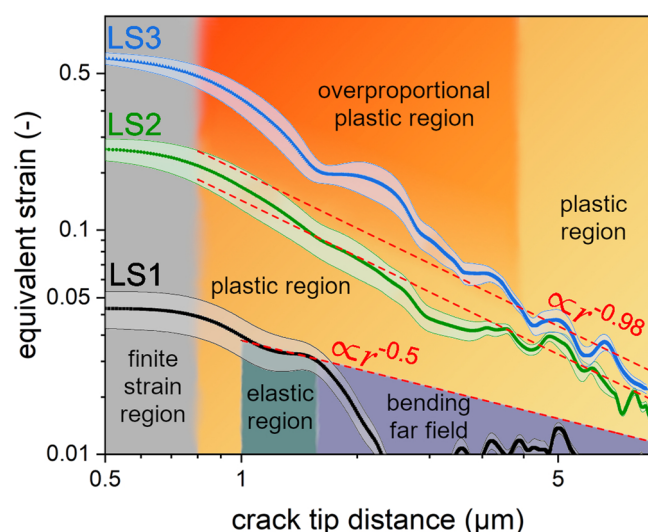
Fig. 3 | Evolution of the equivalent crack tip strains. Double logarithmic plot of average equivalent strain in the highly deformed regions ($\pm30°-60°$) in front of the crack tip for each loading step. The transparent bound depicts the respective standard errors for each crack tip distance, while dashed lines act as guides for the eye and indicate the strain dependency necessary for valid K- ($r^{-0.5}$) or HRR- ($r^{-0.98}$) descriptions, respectively.

Generally, at LS1, the comparison between the experimental data and the FE-model yields excellent agreement outside the immediate crack tip vicinity (see Supplementary Fig. S14, Fig. 5a and d). The lower experimental von Mises stress magnitudes directly in front of the crack tip (Fig. 5g) may be related to the (i) finite notch radius obtained by the focused ion beam cantilever preparation, (ii) the finite X-ray gauge volume and (iii) the potentially slightly exaggerated experimental σ_{xx} magnitudes.

After loading to 45 mN (LS2), the strain in front of the crack tip significantly increases, in overall agreement with the HRR model ($r^{-0.98}$, for $n = 50$, see Supplementary Note 1)[5,24], but again deviating near the crack tip indicating a region of finite deformation. Stress values around the notch suggest the crack tip vicinity ($<1\,\mu m$) being governed mainly by plastic deformation, aligning with HRR theory[6,7] (Fig. 4b). The PST ratio in LS2 rises towards the crack tip, indicating ideal plastic deformation (Fig. 4e), which is confirmed by the frequency distribution of the PST ratio (Fig. 4h).

Additionally, the stress triaxiality T indicates higher hydrostatic tensile stress components near the crack in a circular zone extending $\sim 5\,\mu m$ ($T > 1/\sqrt{3}$), consistent with plastic deformation and potential void formation (Fig. 4k). However, up to $1\,\mu m$ from the crack tip T amounts below 2, in good agreement with the range of the HRR field identified in Fig. 4b, indicating plastic deformation and likely onset of void formation in front of the crack tip.

Also, at LS2, the comparison between the experimental data and the FE-model yields very good agreement outside the immediate crack tip vicinity (Supplementary Fig. S4b and e, Fig. 5b and e). Compared to LS1, the deviations of the experimental and modeled $\sigma_{von\ Mises}$ magnitudes increase, while the overall trend of increasing $\sigma_{von\ Mises}$ magnitudes towards the crack tip remains similar for both experiment and model.

At LS3, the strains near the crack tip increase further, reaching about 0.5 and deviating substantially from the theoretical slope of $r^{-0.98}$ [5–7] up to a crack tip distance of $\sim 4\,\mu m$ (Fig. 3). The observed stress values (Fig. 4c) are drastically reduced and differ significantly from each other ($COS > \sigma_{xx} > GDS$), favoring plastic deformation over crack growth in front of the crack tip (cf. Fig. 4l). The distinct zones of plastic, elastic, and bending-dominated regions blend together, showing continuous transitions (Fig. 4c). The PST ratio increases further at LS3 (Fig. 4f), which indicates complete plastic deformation[52] and suggests even some major pore formation due to

the average exceeding the 0.5 threshold (Fig. 4i) from constant incompressible volume arguments[53], in agreement with the pores found by the post-experiment SEM analysis (Supplementary Note 2). Additionally, T decreases near the crack tip (Fig. 4l), substantiating plastic deformation rather than crack growth.

At LS3, the FE-model yields further increase of the $\sigma_{von\ Mises}$ stress magnitudes as can be drawn from Fig. 5c. The differences are for the first time clearly not only restricted to the immediate crack tip area (Fig. 5c and f). Furthermore, the effect of strain softening is highlighted in the experimental data, where in contrast to the model, $\sigma_{von\ Mises}$ decreases with decreasing distance from the crack tip (Fig. 5i). It is worth to remind that the FEM model employed the Ramberg-Osgood hardening fit to the experimental tensile data (Supplementary Note 1) as a constitutive law, which can not account for the strain softening—this explains such a mismatch in this region.

J-integral calculations

The incrementally calculated J-integral J_{iter} (see Supplementary Note 7) from experimental load-displacement data is given in Fig. 6a with open black squares, exhibiting a roughly linear relationship with crack extension up to 3.5 μm, after which the slope increases significantly. This increase in slope is rather non-physical in the general J-integral framework and indicates a transition from crack extension to general plastic deformation[54].

The analytical J-integral values enumerated from the combined SEM-DIC strain data and the CSnanoXRD stress data, J_{comb} (Eq. 4), are shown for each loadstep in Fig. 6b–d, respectively. The data are depicted for each ellipsoidal contour width (8 μm: green squares, 16 μm; orange circles, 24 μm; purple triangles) and different strain energy density calculation (plastic strain: filled symbols, elastic stress: open symbols) with respect to contour distance from the crack tip as schematically shown in Fig. 1b. For the mainly elastic case at LS1 the J-integral data slightly increases for contours very close to the crack tip, transitioning to a constant regime between 3–4 μm crack tip distance. In this case the elastically calculated data are lower than the plastically calculated data and even lead to unphysical negative J-integral values (minimum $-57 \pm 25\ J\cdot m^{-2}$ for the 8 μm contour). However, considering the significant scatter and small absolute values a general agreement between plastic and elastic evaluation can still be stated. Furthermore, all contour widths agree amongst themselves, suggesting validity of the calculation and a path independence of the J-integral given a sufficiently large contour around the crack tip. For evaluation purposes the average plastically calculated values at a path-independence threshold of 5 μm crack tip distance are summarized in Table 1. LS2 (Fig. 6c) shows a strong decrease of J-integral with contour distance and a higher stable value for the 8 μm width compared to the 16 μm and 24 μm contours (Fig. 6c). However, purely elastic and plastic strain energy density calculations depict an overall agreement regarding the data trends. The maximum discrepancy of the average J-integral in the 5–13 μm range between the evaluation schemes is 131 $J\cdot m^{-2}$, with the elastic evaluation generally lower for all contours. LS3 showed over proportionally high J-integral values up to 4000 $J\cdot m^{-2}$ for the closest crack tip contours (between 0.5 and 2.8 μm, not shown due to scaling), which decrease rapidly with increasing contour - crack tip distance, followed by a nearly stable J-integral regime within a high scatter bound in the 5–13 μm range (Fig. 6d). The smallest contour width (8 μm: green squares) exhibits a minimum of $J_{comb} \approx 1300\ J\cdot m^{-2}$ around 6 μm crack tip distance, with a slight increase towards a stable J-integral plateau with an average of $1530 \pm 126\ J\cdot m^{-2}$. In comparison, the 16 μm and 24 μm contours average at $645 \pm 138\ J\cdot m^{-2}$ and $612 \pm 136\ J\cdot m^{-2}$, respectively. This suggests a strong path dependence of the J-integral within the highly plastically deformed region around the crack tip. General agreement between elastic and plastic evaluation schemes is again evident, but the trend for a lower elastic evaluation is not apparent anymore. Contrarily to LS1 and LS2, the average elastically evaluated 8 μm contour width J-integral is even slightly higher than the plastically evaluated one, being $1554 \pm 114\ J\cdot m^{-2}$. While this difference is negligible in comparison to the scatter, it provides

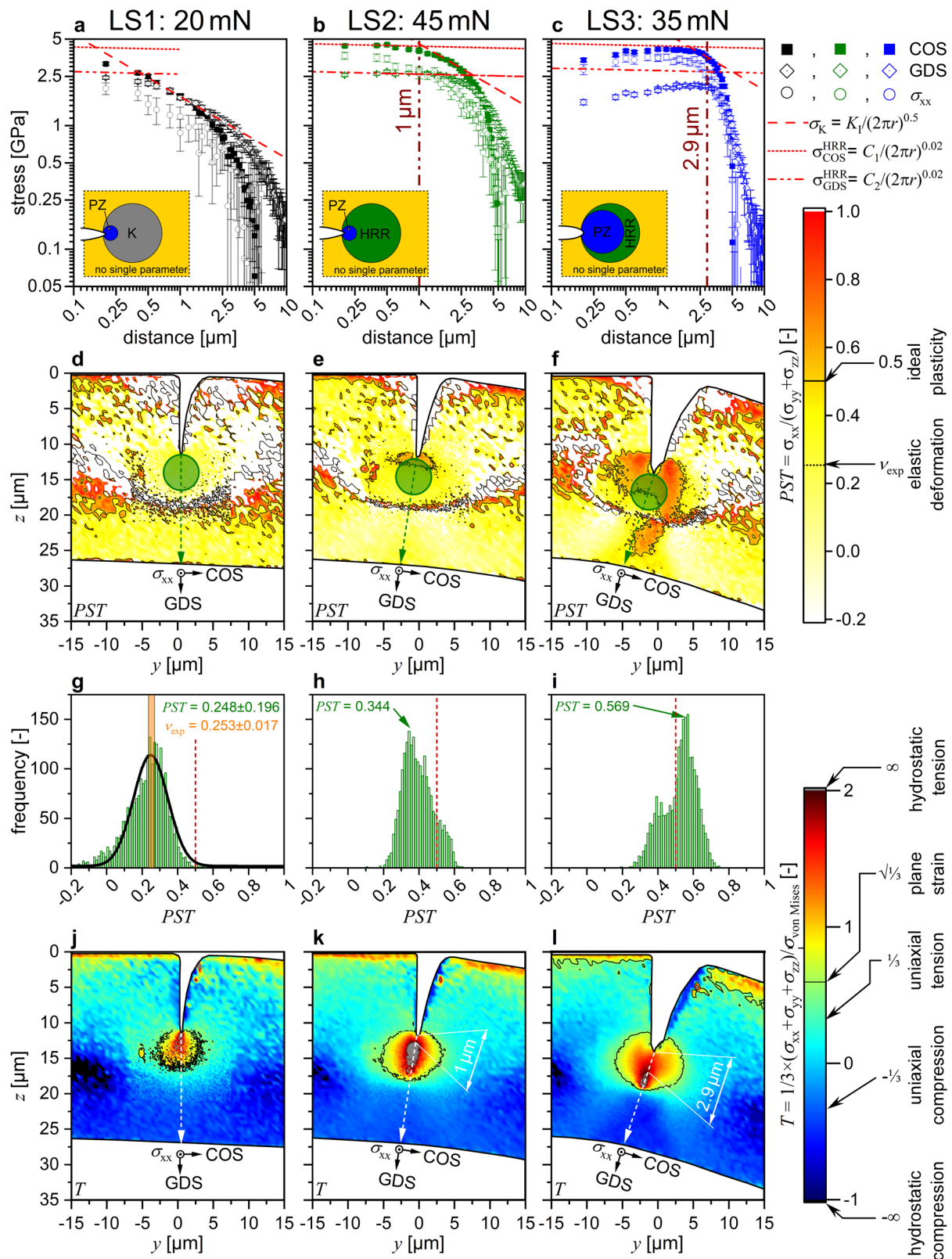**Fig. 4 | Crack tip stress characteristics upon loading.** The crack opening stresses (COS), growth direction stresses (GDS) and σ_{xx} are shown for LS1, LS2, and LS3 in (**a**–**c**), respectively. The PST value introduced in Eq. 2 to verify the evaluated crack tip stresses is presented in (**d**–**f**), respectively, where the black contour line marks PST = 0.5, which can be attributed to full plastic deformation. Additionally, circles with a diameter of 5 μm in front of the crack tip represent the area from which values were taken for the statistical analysis shown in (**g**–**i**). Additionally, Poisson's ratio $v_{exp} = 0.253 \pm 0.017$[24] for this HEA is indicated in (**g**). Finally, in (**j**–**l**) the triaxiality ratio, being the relation between the hydrostatic portion of the stress tensor and the von-Mises stress representing the strain energy of distortion, is shown. The black contour line in (**j**–**l**) corresponds to $T = 1/\sqrt{3} \approx 0.577$, representing a plane strain state. The error bars in (**a**–**c**) depict the standard deviation of the stress results.
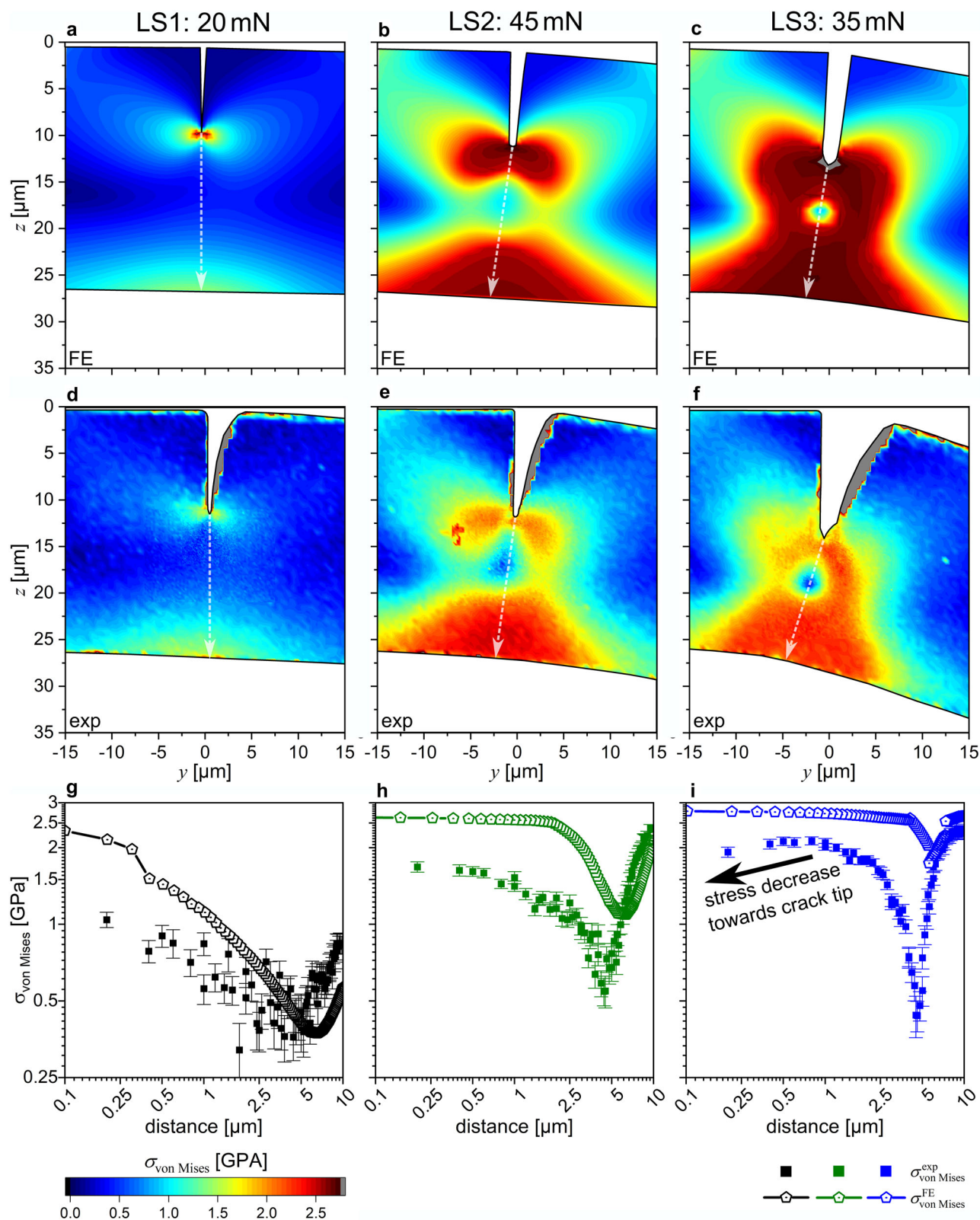
Fig. 5 | Comparison between FE-model and the experimental data. Modeled and experimental $\sigma_{\text{von Mises}}$ distributions are shown in for LS1, LS2, and LS3 in (**a**–**c**) as well as (**d**–**f**), respectively. The evaluated crack tip von Mises stresses are presented in (**d**–**f**), respectively, where the full and open symbols indicate the experimental and modeled data. The error bars in (**g**–**i**) depict the standard deviation of the experimental stress results.

another validity check for the evaluation scheme, as both calculations follow a completely different route but end up at almost equal results.

For comparison, the average plastically evaluated *J*-integral data of all three loadsteps are depicted in Fig. 6a for each contour width, respectively.

The crack extension data was taken from the CSnanoXRD-SAXSM images (*cf.* Figs. 1c and 2c, Supplementary Note 4). The intermediate (16 μm: orange circles) and largest (24 μm: purple triangles) contour widths are in excellent agreement, suggesting actual path independence of the *J*-integral
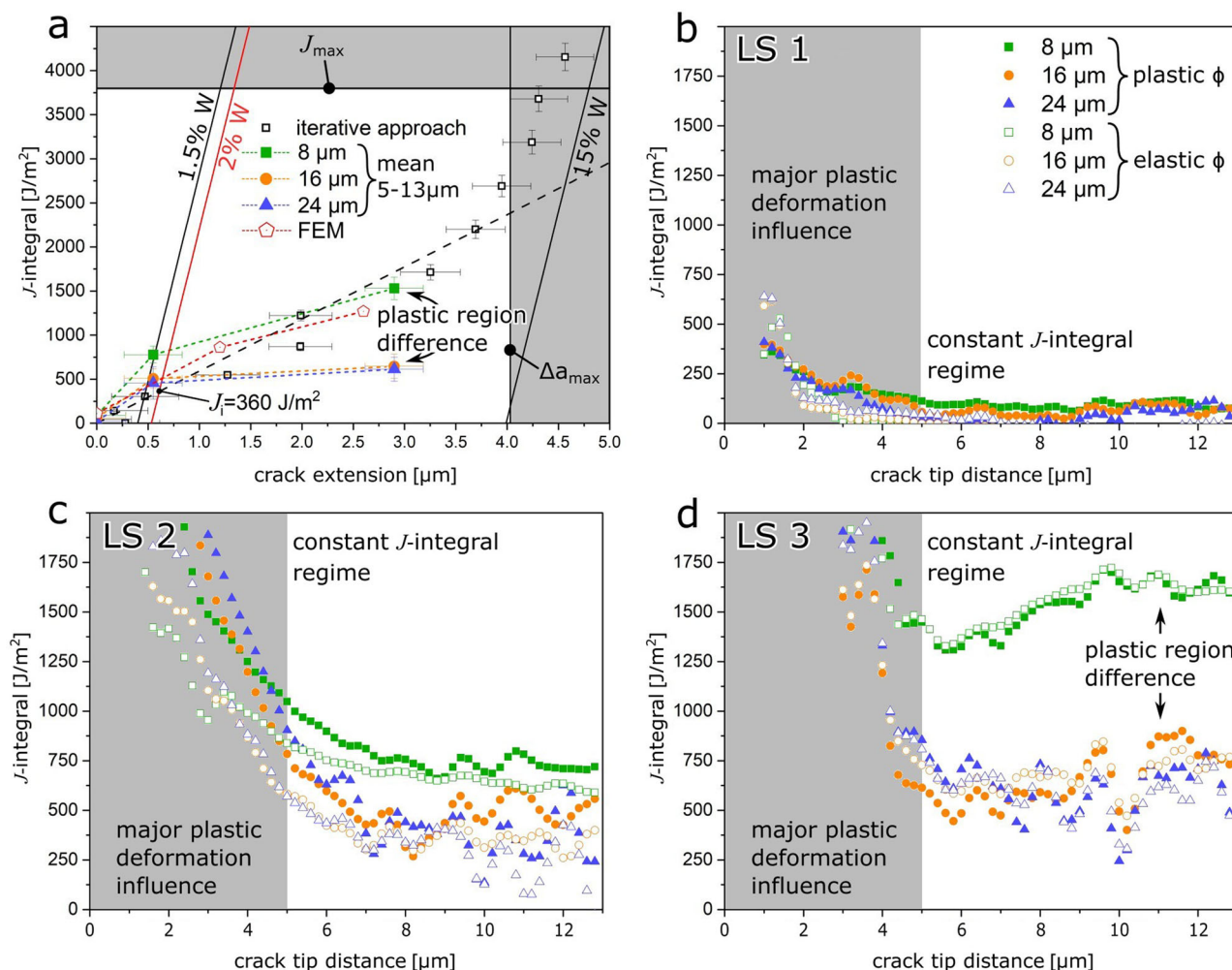
Fig. 6 | J-integral data obtained from the iterative and combined approaches. *J*-integral data from the iterative approach in analogy to ASTM 1820 (open black squares) in conjunction with the contour *J*-integral evaluation for LS1, LS2, and LS3 averaged from 5 to 13 μm crack tip distance as well as data from FE simulations (red pentagons). **a** The individual symbols correspond to small (8 μm: green squares), medium (16 μm: orange circles) and wide (24 μm: blue triangles) integration paths, respectively. Contour *J*-integral data as a function of distance between the crack tip and the elliptic contour are shown using plastic (filled symbols) and elastic (open symbols) strain energy density evaluation for (**b**) LS1, (**c**) LS2 and (**d**) LS3, respectively. The figure legend in (**b**) is applicable for (**c**) and (**d**) as well. The error bars in (**a**) depict the standard deviation of the *J*-integral values in the averaged region for the combined approach and uncertainty propagations from the uncorrelated geometric and mechanical input quantities for the iterative method.

along these contours, while the smallest contour (8 μm: green squares) leads to higher values already at LS2, and more than double the *J*-integral value in the fully plastic case of LS3. In comparison to the incrementally calculated values, all contour *J*-integral values are lower, with only the smallest contour calculation remaining in closer proximity.

Discussion
In contrast to prior approaches[11,12,18,55], the significant advantage of the present work is that for the first time stress and strain results retrieved from the two similarly deformed cantilevers of the same material were combined to evaluate the local *J*-integral along contours in front of the crack tip, which will be discussed in detail hereafter. Full details regarding the agreement between the individual cantilever bending experiments are given in Supplementary Note 2. The following discussion will be divided into two parts, first the transition from linear elastic theory to general yielding will be laid out, while second the validity and the breakdown regimes of the *J*-integral description will be considered.

To facilitate discussion, various approaches for *K*- or *J*-evaluation schemes will be compared, considering mode I loading (Supplementary Note 7), which is appropriate given the K_{II}/K_I ratios evaluated from the FE-model range between 0.058 and 0.073 (Table 1). To circumvent confusion, subscripts will be used to denote the combined stress-strain map contour approach (comb), the iterative sequential unloading approach (iter), the classical linear elastic calculation utilizing load data and specimen geometry (geom), and fitting of the linear COS behaviour in front of the crack tip (COS), respectively. Additionally, the PZ sizes after the respective *K* values as well as measured from the triaxiality maps ($T > 2$, Fig. 4k,l) straight in front of the crack tip[8]. For comparison, all results discussed are summarized in Table 1. After loading the CSnanoXRD cantilever to ~20 mN (LS1), formation of the so-called linear elastic *K*-field around the crack tip is evident, indicated by the negative 0.5 slope in Fig. 4a, surrounding a PZ, extending less than 500 nm. Therefore, no crack extension should be present, and the PZ is likely to contain only a minor amount of plasticity. Utilizing the calculated $J_{comb} = 22$ J·m^{-2} (largest contour, plastic evaluation scheme) for LS1 within the HRR framework would lead to COS trends following the dotted line (Fig. 4a), which does not agree with the measured stresses and provides additional evidence for predominantly elastic loading. Reversing the argument and using the COS data within the linear elastic *K*-framework yields $K_{COS} = 4.3 \pm 0.1$ MPa·m$^{0.5}$. This is in astonishing agreement with simple *K*-evaluation using the load and geometry data (see Supplementary Note 7)[56] during the CSnanoXRD experiment at $K_{geom} = 4.5 \pm 0.2$ MPa·m$^{0.5}$. Similarly, using the corresponding

Table 1 | Summary of *K* and *J* and experimental data

			LS1			LS2			LS3		
SEM			iter	geom		iter			iter		
	K	MPa m$^{0.5}$	5.6 ± 0.2	5.0 ± 0.1		11.0 ± 0.6			19.4 ± 1.0		
	J	J·m^{-2}	142 ± 9	114 ± 5		548 ± 31			1713 ± 87		
	r_p	µm	0.3 ± 0.0	0.2 ± 0.0		1.2 ± 0.1			3.6 ± 0.2		
CSnanoXRD			COS	geom		COS			COS		
	K	MPa m$^{0.5}$	4.3 ± 0.1	4.5 ± 0.2		11.5 ± 0.3			15.3 ± 0.5		
	J	J·m^{-2}	91 ± 5	92 ± 15		604 ± 16			1069 ± 35		
	r_p	µm	0.2 ± 0.0	0.2 ± 0.0		1.3 ± 0.1			2.2 ± 0.1		
	r_p (T ≥ 2)	µm	–			1.0			2.9		
FE-model			Stress field	Average		Stress field	Average		Stress field	Average	
	K_I	MPa m$^{0.5}$	4.5	4.9		13.8	13.7		19.4	16.7	
	K_{II}	MPa m$^{0.5}$	0.3	–		0.8	–		1.5	–	
	J	J·m^{-2}	94	111		866	860		1715	1268	
	r_p	µm	0.2	0.3		1.8	1.8		3.6	2.7	
Combined analysis			8 µm	16 µm	24 µm	8 µm	16 µm	24 µm	8 µm	16 µm	24 µm
	K	MPa m$^{0.5}$	–	–	2.2 ± 4.7	–	–	10.0 ± 4.1	–	–	11.6 ± 2.6
	J	J·m^{-2}	91 ± 15	61 ± 23	22 ± 47	777 ± 94	507 ± 109	456 ± 186	1530 ± 126	645 ± 138	612 ± 136
	r_p	µm	–	–	0.0 ± 0.1	–	–	1.0 ± 0.4	–	–	1.3 ± 0.3

Values obtained from the SEM, CSnanoXRD and modelled cantilevers individually, as well as the combined values for the three contours (8, 16, and 24 µm) according to the evaluation scheme of Supplementary Note 7 and the Methods Section.

load/geometry data of the SEM cantilever, yields K_{geom} = 5.0 ± 0.1 MPa m$^{0.5}$, which is slightly higher than for the CSnanoXRD specimen. This discrepancy between the geometric calculations is a result of slight differences in the cantilever geometries. The iterative calculation based on the load-displacement data yields K = 5.6 ± 0.2 MPa m$^{0.5}$, which is even higher and suggests that some minor amount of plastic deformation is already incorporated into the specimen.

However, this difference clearly highlights the main drawback of the iterative approach: it is not capable of distinguishing between plasticity at the crack tip or elsewhere, e.g. the indenter tip–cantilever contact or the beam base, and can therefore always lead to overestimation based on experimental conditions as detailed in[57,58] and summarized in Supplementary Note 7. The difference between the individual J_{comb} evaluations (largest contour 22 J·m^{-2}, smallest contour 91 J·m^{-2}) is likely a result of the slight discrepancies between local spots on the two different specimens, as well as positioning uncertainties between the stress and strain fields, respectively. However, in comparison to the J magnitudes during further loadsteps (up to 1500 J·m^{-2}), these variations seem minor. As the values are in good agreement with the K estimates and the calculated PZ radii r_p (Table 1) are considerably small in comparison to the overall specimen geometry (max. 0.3 µm), it can be stated that linear elasticity is the governing behaviour during LS1.

After loading to 45 mN the stress slope follows the HRR model and the difference between COS and GDS agrees with this concept (Fig. 4b). In detail, the evaluated σ_{yy} and σ_{zz} distributions calculated from $J_{comb, LS2}$ reach 62% of the stress magnitude of the plane strain assumption[59]. A linear regression between tabulated plane stress and plane strain constants[59] would yield at least ~36% plane strain state in the sample. This contrasts the σ_{xx} (Supplementary Note 4), PST (Fig. 4e, h) and the T (Fig. 4k) data, which all support major plane strain state for large parts of the sample. Possible reasons for these differences may be identified in some degree of mechanical settling, where a certain force (around 10–15% at LS2) is diminished at a given static displacement (Supplementary Note 2). However, independent of the actual percentage of the 2D plane strain assumptions, the results favourably agree with the HRR model in the PZ and depict an evident transition from the linear-elastic to an elastic-plastic case. Similarly, the

equivalent strain decreases with an $r^{-0.98}$ slope at crack tip distances larger than 1.5 µm (Fig. 3), further supporting the HRR-type deformation case. Given the fact that LS2 agrees favourably with rather simplified theoretical predictions underlines the fact that the nanocrystalline HEA can indeed be considered to undergo quasi-ideal isotropic deformation up to this loading stage, following a Ramberg-Osgood type hardening law (Fig. 4b).

Further loading increases the strain accumulated in front of the crack tip (Fig. 3, Supplementary Note 3), while simultaneously the stress significantly diminishes (Fig. 4c, Supplementary Note 4). Especially the triaxiality (Fig. 4l) and the normal stress distributions in front of the crack tip (Fig. 4c) underline that the crack tip singularity HRR-field calculated from $J_{comb, LS3}$ = 612 J·m^{-2} is not valid anymore, since both COS and GDS do not reach the values calculated from the HRR model. While this stress reduction effect might point to void formation at the crack tip and individual large voids coalescent with the crack surface were found by ex situ SEM analysis, the lack of an increased signal in the SAXSM data ahead of the crack (*cf.* Fig. 2c and Supplementary Note 4) suggests only limited increase in free surfaces, i.e., voids. Though the reduction of the individual stress components towards the crack tip (Fig. 4c) may be related to crack tip blunting and is also well recreated by the FE-model (Supplementary Fig. S14f). Since at LS3 the FE model follows Ramberg-Osgood hardening, further increase of $\sigma_{von\ Mises}$ towards the crack tip is observed (Fig. 5i). This is in stark contrast to the experimental data, where a decrease of $\sigma_{von\ Mises}$ towards the crack tip at LS3 was evaluated (Fig. 5i). Thus, in agreement with the micromechanical data of the exact same HEA[24] (Supplementary Note 1) the observed decrease of $\sigma_{von\ Mises}$ might rather be resultant of the unconventional true strain-softening. Conversely, true strain softening[47,60,61] is regularly observed in nanocrystalline metals processed by severe plastic deformation and was also found for this material[24] (Supplementary Note 1). According to literature, strain softening is related to (i) easier dislocation nucleation due to local residual stress fields of remaining dislocation cores at grain boundaries[62], (ii) a very large amount and area fraction of high-angle grain boundaries acting as dislocation sinks[47] or to (iii) slight grain growth[63]. Here, the latter two possibilities concur with the observed decrease of the FWHM with ongoing deformation (Fig. 2d and Supplementary Note 4), further strengthening the argument for true strain-softening. The immediate consequence is that the

$J_{\text{comb, LS3}}$ calculated along the innermost path with a diameter of 8 μm settles at a higher J value of 1760 J·m^{-2} and thus shows a path dependency even outside the closest crack tip vicinity. Additionally. excess plastic deformation is indicated by the rapidly increasing J_{iter} evaluated from sequential unloading (Fig. 6a).

Finally, J_{comb} settles only outside the crack tip-induced stress/strain fields (compare Figs. 2–4 with Fig. 5), yet yields comparable results for J as in LS2. Given that the experimental stress and strain data suggest general yielding at LS3, it is obvious that J_{comb} becomes path-dependent, as the stress-strain fields do not fulfil the requirements for the J-integral approach, with a minimum contour of 16 μm width at a crack tip distance of 4 μm. The resulting implications of validity and breakdown of the J-integral description in fracture mechanics will be discussed next.

Computing the J-integral from theoretical elastic and elastic-plastic stress and strain models (i.e., the K- and the HRR-fields, respectively) should generally yield a J_{comb} value independent of the integration path radius r. To date, only finite element simulations have been used to investigate the near crack tip vicinity and study any potential breakdown of path-independence of the J-integral[64,65]. However, these simulations show a decrease in J towards the crack tip, opposite to the experimentally observed increase presented here (*cf.* Fig. 6b–d). Possible experimental influences leading to such a behaviour would include (i) an imprecise positioning of the notch tips in the CSnanoXRD or SEM experiment, (ii) inadequate elastic constants for the stress calculation and (iii) deviations of the strain due to different strain/stress states at the surface compared to the bulk. However, the stress data shown in Figs. 2 and 4 and the supporting information fits very well to the elastic ($COS \propto r^{-0.5}$) and elastic-plastic ($COS \propto r^{-0.02}$) models established in literature[6–8] for LS1 and LS2, respectively. This suggests general validity of the results and therefore only negligible errors regarding (i) crack tip position, while (ii) different elastic constants would shift the stress state. However, the bending stress component far off the notch in LS1 is in good agreement with geometrical considerations, while the σ_{yy} far off the notch is in excellent agreement with the elastic-plastic FE model for both LS1 and LS2, indicating rather adequate elastic constants (Supplementary Notes 4 and 7). Finally, the difference between plane-strain and plane-stress state cases in the K and HRR crack tip models only results in different pre-factors (different offsets in the double logarithmic plots), but analogous exponents (similar slopes in double logarithmic plots), which would lead to a constant shift in J-integral, again independent of crack tip distance.

Therefore, the only reasonable explanation for such an increase in J_{comb} towards the crack tip is a true strain deviating from the models (ε not proportional to $r^{-0.5}$ or $r^{-0.98}$ for linear elastic and elastic-plastic loading, respectively (Fig. 3)). To regard this trend in a rigorous mathematical context, we argue that both terms within the J-integral (Eq. 4) are proportional to stress-strain products, so estimating a circular contour ($\varphi = [0, 360°]$) around a crack tip in a Ramberg-Osgood type hardening material (HRR field), yields a proportionality as:

$$J \propto \int_{\Gamma} \sigma \cdot \varepsilon \cdot r \cdot d\varphi \propto \int_{\Gamma} r^{-\frac{1}{n+1}} \cdot r^{-\frac{n}{n+1}} \cdot r \cdot d\varphi \propto \int_{\Gamma} \frac{1}{r} \cdot r \cdot d\varphi \quad (1)$$

Therefore, no dependence with crack tip distance r should be present. However, if the strain was to increase with a disproportionally larger magnitude towards the crack tip, this estimation would not hold anymore, and an increase of J in regions of higher strain will be resultant.

This behaviour is verified by the strong discrepancy in the different contour data in Fig. 6a and d, where in the case of the narrowest contour (8 μm) part of the integration will always include over-proportional increased strain, analogous to Fig. 3, where the slope of LS3 (in the 4 μm crack tip vicinity) is evidently higher than the $r^{-0.98}$ proportionality. Furthermore, as shown in Fig. 4c, at LS3 neither K nor HRR crack tip stress fields are well represented by the stress data, suggesting a case of general yielding[1,6–8]. Thus, in this configuration the J-integral formulation is not valid once the integration contour is within the highly plastically deformed region around the crack tip. Additionally, the decreasing triaxiality towards

the crack tip indicates that the stress state favours plastic deformation over void formation and fracture. The reason for this behaviour lies in the initial material properties of the nanocrystalline HEA alloy, which is saturated with defects before loading due to the HPT processing. This leads to defect removal during loading and indicate a true-strain softening material, supported by the FWHM microscopy data evaluated from the CSnanoXRD experiment (Supplementary Note 4) and the uniaxial stress-strain data[24], where the true stress decreases at further (true) strain accumulation. Strain softening is regularly found in ultra-fine grained and nanocrystalline materials[47,60,61] and related to (i) easier dislocation nucleation due to local residual stress fields of remaining dislocation cores at grain boundaries[62], a very large area of high-angle grain boundaries acting as dislocation sinks[47] or (iii) slight grain growth[63]. While for the first possibility, strains of 2$^{\text{nd}}$ order would rise the FWHM, the latter two possibilities concur with a decrease of the FWHM with ongoing deformation (Fig. 2d and Supplementary Note 4). In this case, further accumulation of plasticity would lead to defect annihilation at the crack tip, subsequent softening and thus an over-proportional increase in strain magnitude upon loading.

In comparison to the common iterative approach often conducted in micromechanical testing (Fig. 6a,[57,66]) it is evident that both the J-integral magnitude as well as the crack extension are considerably overestimated in the later part of the experiment (LS3). This can be attributed to plasticity, which is not solely governed by the crack tip, e.g. contains also deformation at the cantilever base, the compressive fibre at the ligament, or the wedge tip-cantilever contact. All of these factors can influence the stiffness and therefore the crack extension measurement as well as the load-displacement response, which directly relates to the calculated J_{iter}. However, considering LS2 where the HRR field description still holds (Fig. 4b) and the J-integral acts as valid crack tip loading parameter, the agreement with the iterative approach is astounding (Table 1). However, this agreement is restricted to identifying the onset of crack growth, while taking the same load-displacement data as for the iterative approach yields significantly over-estimated crack growth and J-integral values by the iterative approach compared to the combined data (Fig. 6a). Consequently, the apparent restriction in the present case is a sufficient crack tip integration distance of ~5 μm at a lateral expansion of 16 μm (Fig. 6c and Table 1), but in general, this depends on the material, specimen size and external loading parameters.

Therefore, the comparatively simple iterative approach can still be used to determine a conservative scalar fracture characteristic for the onset of crack extension, even for non-conventional systems, such as highly plastically deforming or even strain softening materials alike the nanocrystalline HEA studied here. Nevertheless, the iterative approach fails completely to describe the aspects of plastic failure in the HEA, which includes pore formation and coalescence with the crack tip (Supplementary Note 2) and the effects of strain softening (Supplementary Note 1) resulting in path dependence of the J-integral. Subsequently, the iterative J-integral is over-estimated by at least a factor of 3, while crack growth is exaggerated up to 50% (Fig. 6). In following, if a detailed investigation on the crack growth resistance is the aim of any study, it is evident that the iterative approach does not deliver reliable results and more elaborate experimental methods, such as introduced herein, are necessary for any rigorous assessment. Additionally, with ongoing miniaturization of modern materials systems, individual mechanically relevant constituents may not extend to the critical dimensions necessary for a valid J-integral description as shown in this study, while testing conditions probably introduce plasticity elsewhere in the sample. Furthermore, the here presented results hold true not only for the case of the nanocrystalline HEA presented here for the broader case of nanocrystalline materials (with the capability for plastic deformation), most of which show softening during deformation[47,60,61]. Finally, the findings of this study hold even further truth in the case of modern structural (and functional) materials or technologically relevant heterogeneous devices, which may show distinctive mechanical behaviour not covered by the Ramberg-Osgood law[5], such as secondary phases[33], dislocation multiplicity[26] or dynamic competition of screw and edge dislocations[28].

Given the experimental progress demonstrated in this study, future possibilities of combined stress and strain evaluation in front of crack tips include technologically highly relevant semi-ductile materials such as high-strength steels[67–69] or Ti alloys[70,71] which can exhibit brittle fracture after certain amount of plastic deformation. The unique possibilities of the combined in situ SEM and CSnanoXRD approach will further enhance understanding of the partitioning of stresses and strains and their association with fracture in ductile or semi-ductile materials, even across interfaces or in gradient materials. Further experimental improvements will be enabled by much higher scan rates during the in situ CSnanoXRD experiment at 4th generation synchrotron radiation facilities[72,73] and the application of multi-layer Laue lenses (MLLs)[74,75]. While the former allows for faster data generation and thus more investigated loadsteps, the latter enables focussing the X-ray beam below 100 nm in diameter, thereby further enhancing the spatial resolution of the X-ray experiment[74]. While the correlated SEM experiments enabled the strain determination in the present investigation, the caveat of having similar and quasi-isotropic, but still two individual, rather than one unique specimen, remains. However, the feature-based strain mapping as presented herein is not limited to SEM imaging. Thus, using single experiments and advanced image formation capabilities (SAXS and FWHM microscopy) during CSnanoXRD experiments will remove any potential doubts regarding differences between stress and strain data in the future.

Conclusions

This work presents the first experimental evaluation of the elastic-plastic fracture parameter J_{comb} in front of a crack tip with previously unseen deep sub-micron resolution. The unique methodology developed here allowed for the separate analysis of strain and stress in a nanocrystalline FeCrMn-NiCo HEA alloy. The experimental results detail the transition from linear elastic loading via elastic-plastic deformation to general yielding, in agreement with respective theoretical concepts. Thereby, we demonstrate that even in the case of a valid HRR field the path independence of the J-integral is not given in a rather large crack tip vicinity of several microns, especially for the strain-softening nature of the nanocrystalline material studied herein. In the case of general yielding, the J-integral obtained by the sequential unloading method significantly deviates from the one obtained from actual stress and strain fields, which is related to true strain softening of the nanocrystalline HEA. In turn, the J-integral becomes also path dependent, even outside the crack tip vicinity. Consequently, the J-integral is no longer a valid description of the crack growth resistance beyond the onset of fracture in state-of-the-art elastic-plastic materials both when deviating from a simplistic Ramberg-Osgood hardening behaviour and at the microscale. These findings underline the importance of refined fracture mechanical concepts and experimental analysis schemes considering crack growth resistance for assessing the damage tolerance of advanced materials on a local scale.

Materials and methods
Material preparation
The material used in this study is an equiatomic five-component CoCr-FeMnNi HEA, commonly known as the Cantor alloy[36,37], which was processed by HPT under the same technical parameters (pressure, strain-rate and temperature) as described by Schuh et al.[37] to achieve a nanocrystalline microstructure with a grain size of 50 nm. A wedge-shaped specimen was prepared from the HPT disk by grinding and careful polishing to a final thickness of ~40 μm leading to a specimen orientation with the crack propagation direction in the radial direction and the crack plane normal pointing in the tangential direction.

Femto-second laser and focused ion beam sample preparation
An Auriga laser[76] system (Carl Zeiss AG, Oberkochen, Germany), combining focused ion beam (FIB) milling and femtosecond laser ablation (Origami 10 XP, Onefive GmbH, Regensdorf, Switzerland) was used to fabricate the notched freestanding cantilevers of $W \times B = 26.2$–26.5 μm × 28–29 μm, with L chosen in such way that a similar nominal stress intensity is applied for both cantilevers. The initial notch depth was ~9 μm, to obtain single defect-controlled specimens with a/W ~ 0.3 as common in small-scale fracture investigations. Full details about the specimen fabrication routine can be found in Supplementary Note 6.

Scanning electron microscopy imaging
Cantilevers for in situ SEM and CSnanoXRD experiments were imaged prior and after the testing in a field emission SEM (ZEISS LEO1525, Carl Zeiss AG, Oberkochen, Germany) using the in-lens secondary electron detector at an acceleration voltage of 5 kV and an aperture size of 30 μm.

In situ SEM-DIC experiment
A cantilever specimen was tested in situ in a field emission SEM (DSM982, Carl Zeiss AG, Oberkochen, Germany) utilizing an UNAT-SEM 1 micro-indentation device (ASMEC GmbH, Dresden, Germany) equipped with a conductive diamond wedge (Synton MDP, Nidau, Switzerland). The cantilever bending experiment was conducted in displacement-controlled mode with a loading rate of 50 nm/s and sequential unloading steps at every for every 2 μm displacement. To assure a quasi-continuous acquisition of images, the SEM was adjusted to a scan speed requiring 660 ms per frame, which provided a good trade-off between image quality in terms of signal-to-noise and temporal resolution[24]. The iterative J-integral is calculated as presented in ref. [57]. As the evaluation of a proper crack growth initiation toughness at the microscale cannot be directly evaluated using macroscopic standards (e.g. ASTM1820[77]), the 2%W (ligament width) translation criterion, proposed by Pippan et al. [58], was used. This is shown in Fig. 6a, where blunting lines with slopes of $2\sigma_y = 4710$ MPa[24] are drawn for 1.5%, 2%, and 15% W offsets, respectively. In macroscopic experiments, the data between the 1.5% and 15% W offsets would count as valid for a fitting procedure, whereas the intersection of the fitted line with the 2% W line indicates the crack growth initiation toughness. Furthermore, additional invalidity criteria for J-integral testing are the maximum J-integral capacity $J_{max} = (W - a_0) \cdot \sigma_y /10 = 3796$ J · m^{-2} and maximum crack extension capacity $\Delta a_{max} = 0.25 \cdot (W - a_0) = 4.03$ μm. Using these criteria as shown in Fig. 6a with a linear fit of the data results in a conditional crack growth initiation toughness $J_i = 360$ J · m^{-2}. The determination of the 2D surface Green-Lagrange strain tensor by point feature tracking is conducted on quasi-continuous SEM images during the experiment, as described in ref. [24]. Additionally, the strain parallel to the crack tip direction ε_{xx} was estimated based on volumetric invariance of the individual quadrilaterals to obtain a quasi-3D representation of the surface strain state. The measured displacement fields are processed using a novel smoothing algorithm based on total variational regularization with a regularization strength of 10^{-2} (cf. Supplementary Note 8 and Supplementary Fig. S18). To assess the stochastic scatter of this methodology, the strain field in crack opening direction ε_{yy} was evaluated from the first to the second frame of the SEM-DIC experiment, which is still out of contact of the indenter. All 3311 evaluation points of this frame were plotted as histogram and used to determine a purely noise dominated normal distribution of ε_{yy}. The mean and standard deviation of this distribution were calculated as $-3.1 \times 10^{-5} \pm 2.9 \times 10^{-4}$, showcasing the very good agreement with the unstrained condition, i.e. $\varepsilon_{yy} = 0$ and a statistic estimate on the average strain value errors of approx. 3×10^{-4}.

In situ CSnanoXRD experiment
The CSnanoXRD experiments[78,79] (Fig. 1a, c) were performed at beamline ID13 of the European Synchrotron (ESRF) in Grenoble, France[74] using a dedicated indenter setup developed for in situ indentation experiments[80]. Compound refractive lenses[81] were used to focus the X-ray beam with a photon energy of 15.2 keV to a spot size of ~150 nm in diameter and a focal depth of ~50 μm. After aligning the sample perpendicular to the incident X-ray beam (cf. supporting information), the cantilever was incrementally loaded to 22, 45, and 36 mN (cf. Supplementary Fig. S1), denoted as load-steps LS1, LS2, and LS3, respectively, and three areas of interest, sized

$30 \times 35\ \mu m^2$, $14 \times 10\ \mu m^2$ and $6 \times 5\ \mu m^2$ were characterized in detail by mesh scanning the sample along the y- and z- direction in 500, 200, and 100 nm steps, respectively, for each of the three loadsteps. Note that the extent of the X-ray gauge volume is equal to the cantilever width B along the x-direction. During the in situ CSnanoXRD experiment 8933 2D diffractograms per loadstep (LS1–LS3) were recorded using an Eiger X 4 M (hybrid photon counting) HPC detector. Additionally, before and after the experiment, further denoted as LS0 and LS4, respectively, the largest areas of interest of $30 \times 35\ \mu m^2$ size were scanned along the y- and z- direction with a decreased step size of 200 nm, resulting in 26576 recorded 2D diffractograms each. The, along the x-direction volume-averaged, 2D diffraction signal was recorded by a Dectris Eiger X 4 M HPC detector at each measurement position using an acquisition time of 50 ms at a sample-to-detector distance of 132.47 mm.

The scattered signal around the beam stop, i.e., small-angle X-ray scattering (SAXS) (Fig. 1c) originates primarily from electron density variations, such as alternation of materials, presence of grain boundaries, interfaces, cracks, precipitates and pores with sizes of $\sim \lambda/\theta$ where λ represents the X-ray wavelength and θ is the Bragg angle[46,82]. Using so-called SAXS microscopy (SAXSM)[46], micrographs primarily sensitive to the intercrystalline defect density were collated to quantitatively evaluate the volumetric crack length averaged over the cantilever thickness B for the individual loadsteps. The arithmetically averaged direction-dependent FWHM[19] were collated to a micrograph for each load step, yielding a vital qualitative parameter to determine the defect accumulation around the crack in the in situ experiment.

The unstressed lattice constant of the face-centered cubic (fcc) HEA was determined from diffraction data near the surface of the cantilever before loading (LS0), considering the stress-free out-of-plane (z) orientation and found to be $a_0 = 0.35928$ nm, according with literature[50]. The evaluation of the 3D stress distributions (i.e., the full stress tensor) was performed using the approach from refs. 18,83. X-ray elastic constants were adopted from literature[84]. The evaluation of the 3D stress tensor was supported by using the diffracted intensities from the 111 and 200 Debye-Scherrer rings, as they have highly different X-ray elastic constants, a consequence of the high crystallographic anisotropy represented by a Zener ratio of $Z = 4.2$[84,85]. Therefore, the individual ring's changes $2\theta(\delta)$ pursuant to the stress tensor are significantly different (cf. supporting information), which in turn allows to retrieve σ_{xx}. Further details on evaluation and experimental constraints can be found in Supplementary Note 9.

Calculation of stress indicators for data interpretation

As a verification for the $\sigma_{xx}(y,z)$ values obtained, a test for the plane strain condition was adopted as follows

$$PST = \frac{\sigma_{xx}(y,z)}{\sigma_{yy}(y,z) + \sigma_{zz}(y,z)}, \qquad (2)$$

where the PST is the ratio between the normal stress component along the incident beam, $\sigma_{xx}(y,z)$ divided by the sum of the normal stress components ($\sigma_{yy}(y,z)$, $\sigma_{zz}(y,z)$) perpendicular to the incident X-ray beam (cf. Fig. 1). For purely elastic loading in front of the crack tip, the PST value should coincide with the Poisson's ratio of the Cantor alloy, which is $v_{exp} = 0.253 \pm 0.017$ as experimentally obtained in[24]. During further loading and concomitant plasticity in front of the crack tip, the PST value should increase towards 0.5, which represents incompressible volume conserving deformation, full plastification of the material[52,53], while values above 0.5 indicate a deviation from conserved volume, e.g. void formation[86].

The triaxiality ratio $T(y,z)$[51] was calculated by dividing the hydrostatic component of the stress tensor $\sigma_H(y,z)$ by the von Mises stress $\sigma_{von\ Mises}(y,z)$

$$T(y,z) = \frac{\sigma_H(y,z)}{\sigma_{von\ Mises}(y,z)}, \qquad (3)$$

where $\sigma_H(y,z) = \frac{1}{3}\left(\sigma_{xx}(y,z) + \sigma_{yy}(y,z) + \sigma_{zz}(y,z)\right)$ is the 1st invariant of the stress tensor.

Finite element modelling

A 3D elasto-plastic Finite Element (FE) model was employed to simulate the indentation process of the pre-notched cantilever using the commercial software COMSOL Multiphysics®. The material constitutive law was modelled using a Ramberg-Osgood hardening law (Eq. S1.1) as discussed in Supplementary Note 1. The adopted plasticity formulation accounts for small plastic strains, with the yield function determined by the Von Mises stress criterion. Given the large deformation expected by this test, geometry non-linearities were accounted by a preceding cohesive zone model using the J_i of 360 J·m^{-2} as the strain energy release rate. The mechanical model exploited second-order serendipity hexahedral elements with 20 nodes, having quadratic shape functions with the mesh consisting of 60216 elements

The values of J_{avg}, were obtained using the dedicated algorithm available in COMSOL Multiphysics. This function computes the 2D J-integral at multiple cross-sections along the specimen's thickness, generating a continuous profile of the J-integral. By averaging this profile across the sample's thickness, it is then possible to obtain J_{avg}. Full details of the FE-models parameters and the process are given in Supplementary Note 10.

Calculation of strain energy density and *J*-integral

Obtaining the full local stress state from CSnanoXRD experiments as well as the full local strain state by SEM-DIC experiments enables determination of J-integral values based on the theoretical contour integral definition[4], as:

$$J = \int_\Gamma \phi\ dy - \vec{T}\frac{\partial\vec{u}}{\partial z}ds \qquad (4)$$

where, $\phi = \int_0^{\varepsilon_{eq}} \underline{\sigma}\ d\underline{\varepsilon}$ is the strain energy density, $\vec{T} = \underline{\sigma}\vec{n}$ is the surface traction vector, and $\vec{u}$ is the deformation vector field, while $\underline{\sigma}$ and $\underline{\varepsilon}$ represent the stress and strain tensors, respectively. The integral is calculated along the contour Γ, as shown in Fig. 1b from the lefthand-side crack flank to the righthand-side crack flank, in accordance with common literature[4]. To investigate the path-independence of the J-integral from the experimental data, various elliptical contours were evaluated, with the origin of each curve constant at 3 μm behind the crack tip and varying maximum eclipse points of the contour in 100 nm steps from 1 μm crack tip distance to a maximum of 13 μm crack tip distance. Furthermore, three different contour widths were chosen to study the influence of the contour path through a majority of the PZ (small) or mainly through an elastically loaded regime (wide) as depicted in Fig. 1b.

Strictly speaking, the J-integral evaluation is considered valid only for linear and non-linear elastic material behaviour. This means that the total work that was put into a certain volume should be considered reversible and therefore adds to the stored strain energy density. To address this assumption the strain-energy density ϕ was calculated following two different approaches. On the one hand, $\phi_{elastic}$ was calculated using purely linear-elastic assumptions and only the CSnanoXRD data as:

$$\phi_{elastic} = \frac{1}{2}\underline{\sigma}\ \underline{\underline{S}}\ \underline{\sigma}^T \qquad (5)$$

with $\underline{S}$ being the isotropic compliance tensor. On the other hand, $\phi_{plastic}$ was calculated by numerical integration of the true stress-strain data $\sigma_{uniaxial}$, as previously determined on micro tensile experiments[24], up to an equivalent total strain ε_{eq} as $\phi_{plastic} = \int_0^{\varepsilon_{eq}} \sigma_{uniaxial} \cdot d\varepsilon$, where ε_{eq} is calculated as the von-Mises equivalent strain from the SEM-DIC strain data. This enables a comparison between linear-elastic and non-linear elastic assumptions in the standard J-integral framework. A detailed analysis of the possible error sources during the integration of the experimental data is given in Supplementary Note 11.

References
1. Griffith, A. A. The phenomena of rupture and flow in solids. *Philos. Trans. R. Soc. A Math. Phys. Eng. Sci.* **221**, 163–198 (1920).
2. Kiener, D. & Han, S. M. 100 years after Griffith: from brittle bulk fracture to failure in 2D materials. *MRS Bulletin* **47**, 792–799 (2022).
3. Wells, A. A. Unstable crack propagation in metals: cleavage and fast fracture. In *Proceedings of the Crack Propagation Symposium*, (eds Aeronautical Research Council, Royal Aeronautical Society) vol. 1, 210–230 (The College of Aeronautics, Cranfield, 1961).
4. Rice, J. R. A path independent integral and the approximate analysis of strain concentration by notches and cracks. *J. Appl. Mech.* **35**, 379–386 (1968).
5. Ramberg, W. & Osgood, W. R. Description of stress-strain curves by three parameters. *Natl. Advis. Com. Aeronaut.* **902**, 13 (1943).
6. Hutchinson, J. W. Plastic stress and strain fields at a crack tip. *J. Mech. Phys. Solids* **16**, 337–342 (1968).
7. Rice, J. R. & Rosengren, G. F. Plane strain deformation near a crack tip in a power law hardening material. *J. Mech. Phys. Solids* **16**, 1–12 (1968).
8. Anderson, T. L. L. *Fracture Mechanics, Fundamentals and Applications*. *CRC Press*. https://doi.org/10.1201/9781315370293 (CRC Press, 2017).
9. Steuwer, A., Santisteban, J. R., Turski, M., Withers, P. J. & Buslaps, T. High-resolution strain mapping in bulk samples using full-profile analysis of energy dispersive synchrotron X-ray diffraction data. *Nucl. Instruments Methods Phys. Res. Sect. B Beam Interact. Mater. Atoms* **238**, 200–204 (2005).
10. Withers, P. J. Residual stress and its role in failure. *Reports Prog. Phys.* **70**, 2211–2264 (2007).
11. Robertson, S. W., Mehta, A., Pelton, A. R. & Ritchie, R. O. Evolution of crack-tip transformation zones in superelastic Nitinol subjected to in situ fatigue: a fracture mechanics and synchrotron X-ray microdiffraction analysis. *Acta Mater* **55**, 6198–6207 (2007).
12. Lopez-Crespo, P. et al. Characterisation of overloads in fatigue by 2D strain mapping at the surface and in the bulk. *Fatigue Fract. Eng. Mater. Struct.* **39**, 1040–1048 (2016).
13. Zhang, W. et al. The effect of anisotropic microstructure on the crack growth and fatigue overload behaviour of ultrafine-grained nickel. *Acta Mater* **184**, 225–240 (2020).
14. Ravi, P., Naragani, D., Kenesei, P., Park, J. S. & Sangid, M. D. Direct observations and characterization of crack closure during microstructurally small fatigue crack growth via in-situ high-energy X-ray characterization. *Acta Mater.* **205**, 116564 (2021).
15. Salvati, E., Zhang, H., Fong, K. S., Song, X. & Korsunsky, A. M. Separating plasticity-induced closure and residual stress contributions to fatigue crack retardation following an overload. *J. Mech. Phys. Solids* **98**, 222–235 (2017).
16. Oddershede, J. et al. Measuring the stress field around an evolving crack in tensile deformed Mg AZ31 using three-dimensional X-ray diffraction. *Acta Mater* **60**, 3570–3580 (2012).
17. Coules, H. E., Horne, G. C. M., Abburi Venkata, K. & Pirling, T. The effects of residual stress on elastic-plastic fracture propagation and stability. *Mater. Des.* **143**, 131–140 (2018).
18. Meindlhumer, M. et al. Evolution of stress fields during crack growth and arrest in a brittle-ductile CrN-Cr clamped-cantilever analysed by X-ray nanodiffraction and modelling. *Mater. Des.* **198**, 109365 (2021).
19. Meindlhumer, M. et al. Nanoscale stress distributions and microstructural changes at scratch track cross-sections of a deformed brittle-ductile CrN-Cr bilayer. *Mater. Des.* **195**, 109023 (2020).
20. Lotze, G., Iyer, A. H. S., Bäcke, O., Kalbfleisch, S. & Colliander, M. H. In situ characterization of stresses, deformation and fracture of thin films using transmission X-ray nanodiffraction microscopy. *J. Synchrotron Radiat.* **31**, 1–13 (2024).
21. Schmuck, K., Alfreider, M. & Kiener, D. Crack length estimations for small-scale fracture experiments via image processing techniques. *J. Mater. Res.* **37**, 2848–2861 (2022).
22. Gao, H., Lin, Z., Huang, X., Shang, H. & Zhan, J. In situ measurement of cyclic plastic zone and internal strain response of Q&P steel near fatigue crack tip region based on micro-DIC. *Materials.* **15**, 6114 (2022).
23. Edwards, T. E. J., Maeder, X., Ast, J., Berger, L. & Michler, J. Mapping pure plastic strains against locally applied stress: revealing toughening plasticity. *Sci. Adv.* **8**, 11 (2022).
24. Alfreider, M., Meindlhumer, M., Maier-Kiener, V., Hohenwarter, A. & Kiener, D. Extracting information from noisy data: strain mapping during dynamic in situ SEM experiments. *J. Mater. Res.* **36**, 2291–2304 (2021).
25. Gludovatz, B. et al. A fracture-resistant high-entropy alloy for cryogenic applications. *Science* **345**, 1153–1158 (2014).
26. Wang, F. et al. Multiplicity of dislocation pathways in a refractory multiprincipal element alloy. *Science* **370**, 95–101 (2020).
27. An, Z. et al. Negative mixing enthalpy solid solutions deliver high strength and ductility. *Nature* **625**, 697–702 (2024).
28. Cook, D. H. et al. Kink bands promote exceptional fracture resistance in a NbTaTiHf refractory medium-entropy alloy. *Science* **384**, 178–184 (2024).
29. George, E. P., Raabe, D. & Ritchie, R. O. High-entropy alloys. *Nat. Rev. Mater.* **4**, 515–534 (2019).
30. Ma, D. et al. Phase stability of non-equiatomic CoCrFeMnNi high entropy alloys. *Acta Mater* **98**, 288–296 (2015).
31. George, E. P., Curtin, W. A. & Tasan, C. C. High entropy alloys: a focused review of mechanical properties and deformation mechanisms. *Acta Mater* **188**, 435–474 (2020).
32. Raabe, D., Tasan, C. C. & Olivetti, E. A. Strategies for improving the sustainability of structural metals. *Nature* **575**, 64–74 (2019).
33. Li, Z., Pradeep, K. G., Deng, Y., Raabe, D. & Tasan, C. C. Metastable high-entropy dual-phase alloys overcome the strength – ductility trade-off. *Nature* **534**, 227–230 (2016).
34. Yao, M. J., Pradeep, K. G., Tasan, C. C. & Raabe, D. A novel, single phase, non-equiatomic FeMnNiCoCr high-entropy alloy with exceptional phase stability and tensile ductility. *Scr. Mater.* **72–73**, 5–8 (2014).
35. Zhang, Z. et al. Superlattice-induced oscillations of interplanar distances and strain effects in the CrN/AlN system. *Phys. Rev. B* **95**, 155305 (2017).
36. Cantor, B., Chang, I. T. H., Knight, P. & Vincent, A. J. B. Microstructural development in equiatomic multicomponent alloys. *Mater. Sci. Eng. A* **375–377**, 213–218 (2004).
37. Schuh, B. et al. Mechanical properties, microstructure and thermal stability of a nanocrystalline CoCrFeMnNi high-entropy alloy after severe plastic deformation. *Acta Mater* **96**, 258–268 (2015).
38. Khadem, M. et al. Formation of discrete periodic nanolayered coatings through tailoring of nanointerfaces-Toward zero macroscale wear. *Sci. Adv.* **7**, 1–19 (2021).
39. Atwani, O. El, Vo, H. T., Tunes, M. A., Lee, C. & Alvarado, A. A quinary WTaCrVHf nanocrystalline refractory high-entropy alloy withholding

extreme irradiation environments. 1–12 https://doi.org/10.1038/s41467-023-38000-y (2023).

40. Uchic, M. D., Dimiduk, D. M., Florando, J. N. & Nix, W. D. Sample dimensions influence strength and crystal plasticity. *Science* **305**, 986–989 (2004).

41. Kiener, D., Wurmshuber, M., Alfreider, M., Schaffar, G. J. K. & Maier-kiener, V. Current opinion in solid state & materials science recent advances in nanomechanical and in situ testing techniques: towards extreme conditions. *Curr. Opin. Solid State Mater. Sci.* **27**, 101108 (2023).

42. Dehm, G., Jaya, B. N., Raghavan, R. & Kirchlechner, C. Overview on micro- and nanomechanical testing: new insights in interface plasticity and fracture at small length scales. *Acta Mater* **142**, 248–282 (2018).

43. Jaya, B. N., Kirchlechner, C. & Dehm, G. Can microscale fracture tests provide reliable fracture toughness values? A case study in silicon. *J. Mater. Res.* **30**, 686–698 (2015).

44. Mishra, A. K. et al. Strategies for damage tolerance enhancement in metal/ceramic thin films: Lessons learned from Ti/TiN. *Acta Mater* **228**, 117777 (2022).

45. Raghavan, R., Kirchlechner, C., Jaya, B. N., Feuerbacher, M. & Dehm, G. Mechanical size effects in a single crystalline equiatomic FeCrCoMnNi high entropy alloy. *Scr. Mater.* **129**, 52–55 (2017).

46. Meindlhumer, M. et al. Nanoscale residual stress and microstructure gradients across the cutting edge area of a TiN coating on WC-Co. *Scr. Mater.* **182**, 11–15 (2020).

47. Huang, X., Hansen, N. & Tsuji, N. Hardening by annealing and softening by deformation in nanostructured metals. *Science* **312**, 249–251 (2006).

48. Renk, O. et al. Increasing the strength of nanocrystalline steels by annealing: is segregation necessary? *Scr. Mater.* **95**, 27–30 (2015).

49. Alfreider, M., Issa, I., Renk, O. & Kiener, D. Probing defect relaxation in ultra-fine grained Ta using micromechanical spectroscopy. *Acta Mater* **185**, 309–319 (2020).

50. Laplanche, G. et al. Temperature dependencies of the elastic moduli and thermal expansion coefficient of an equiatomic, single-phase CoCrFeMnNi high-entropy alloy. *J. Alloys Compd.* **623**, 348–353 (2015).

51. Hancock, J. W. & Mackenzie, A. C. On the mechanisms of ductile failure in high-strength steels subjected to multi-axial stress-states. *J. Mech. Phys. Solids* **24**, 147–160 (1976).

52. MacKenzie, P., McKelvie, J., McDonach, A. & Walker, C. A. Measurement of Poisson's ratio through the elastic-plastic transition. *Strain* **22**, 13–19 (1986).

53. Greaves, G. N., Greer, A. L., Lakes, R. S. & Rouxel, T. Poisson's ratio and modern materials. *Nat. Mater.* **10**, 823–837 (2011).

54. Alfreider, M., Bodlos, R., Romaner, L. & Kiener, D. The influence of chemistry on the interface toughness in a WTi-Cu system. *Acta Mater* **230**, 117813 (2022).

55. Lopez-Crespo, P., Peralta, J. V., Kelleher, J. F. & Withers, P. J. In situ through-thickness analysis of crack tip fields with synchrotron X-ray diffraction. *Int. J. Fatigue* **127**, 500–508 (2019).

56. Tada, H., Paris, P. C. & Irwin, G. R. *The Stress Analysis of Cracks Handbook* (ASME Press, 2000).

57. Wurster, S., Motz, C. & Pippan, R. Characterization of the fracture toughness of micro-sized tungsten single crystal notched specimens. *Philos. Mag.* **92**, 1803–1825 (2012).

58. Pippan, R., Wurster, S. & Kiener, D. Fracture mechanics of micro samples: fundamental considerations. *Mater. Des.* **159**, 252–267 (2018).

59. Brocks, W., Klingbeil, D. & Olschewski, J. *Loesung der HRR-Feld-Gleichungen der Elastisch-Plastischen Bruchmechanik* (Bundesanstalt für Materialforschung und -prüfung (BAM), 1990).

60. Hu, J., Shi, Y. N., Sauvage, X., Sha, G. & Lu, K. Grain boundary stability governs hardening and softening in extremely fine nanograined metals. *Science* **355**, 1292–1296 (2017).

61. Edalati, K. et al. Nanomaterials by severe plastic deformation: review of historical developments and recent advances. *Mater. Res. Lett.* **10**, 163–256 (2022).

62. Tang, F. & Schoenung, J. M. Strain softening in nanocrystalline or ultrafine-grained metals: a mechanistic explanation. *Mater. Sci. Eng. A* **493**, 101–103 (2008).

63. He, X., Zhu, L., Liu, J. & An, L. Grain growth-induced strain softening in nanocrystalline magnesium: experiments and modelling. *Mater. Res. Express* **6**, 108002 (2019).

64. Carka, D. & Landis, C. M. On the path-dependence of the J-integral near a stationary crack in an elastic-plastic material. *J. Appl. Mech. Trans. ASME* **78**, 0110061–0110066 (2011).

65. Zhu, X. K. Effects of large plastic deformation and residual stress on the path independence of J-integral for cracks in ductile materials. *Eng. Fract. Mech.* **277**, 108945 (2023).

66. Saxena, A. K., Brinckmann, S., Völker, B., Dehm, G. & Kirchlechner, C. Experimental conditions affecting the measured fracture toughness at the microscale: notch geometry and crack extension measurement. *Mater. Des.* **191**, 108582 (2020).

67. Kim, S. H., Kim, H. & Kim, N. J. Brittle intermetallic compound makes ultrastrong low-density steel with large ductility. *Nature* **518**, 77–79 (2015).

68. Tasan, C. C. et al. An overview of dual-phase steels: advances in microstructure-oriented processing and micromechanically guided design. *Annu. Rev. Mater. Res.* **45**, 391–431 (2015).

69. Koyama, M. et al. Bone-like crack resistance in hierarchical metastable nanolaminate steels. *Science (80-.).* **355**, 1055–1057 (2017).

70. Hu, Y. N. et al. A new approach to correlate the defect population with the fatigue life of selective laser melted Ti-6Al-4V alloy. *Int. J. Fatigue* **136**, 105584 (2020).

71. Zhang, C. et al. Trifunctional nanoprecipitates ductilize and toughen a strong laminated metastable titanium alloy. *Nat. Commun.* **14**, 1397 (2023).

72. Chapman, H. N. Fourth-generation light sources. *IUCrJ* **10**, 246–247 (2023).

73. Li, P. et al. 4th generation synchrotron source boosts crystalline imaging at the nanoscale. *Light Sci. Appl.* **11**, 73 (2022).

74. Keckes, J. et al. 30 nm X-ray focusing correlates oscillatory stress, texture and structural defect gradients across multilayered TiN-SiOx thin film. *Acta Mater* **144**, 862–873 (2018).

75. Kubec, A. et al. Sub 25 nm focusing with a long working distance using multilayer Laue lenses. *J. Instrum.* **13**, 6 (2018).

76. Pfeifenberger, M. J. et al. The use of femtosecond laser ablation as a novel tool for rapid micro-mechanical sample preparation. *Mater. Des.* **121**, 109–118 (2017).

77. ASTM Standard E1820, Standard test method for measurement of fracture toughness, ASTM B. Stand. 1–54 https://doi.org/10.1520/E1820-13.

78. Keckes, J., Todt, J., Meindlhumer, M. & Ziegelwanger, T. In situ mapping of crack progression in nanocrystalline FeCr: nanoscale stress-strain evolution in nanocrystalline microstructure [Data set]. European Synchrotron Radiation Facility. https://doi.org/10.15151/ESRF-ES-514138045 (2024).

79. Rettenwander, D. et al. Scanning and in-situ MLL development for X-ray nanodiffraction on thin film, space and additively manufactured applications [Data set]. European Synchrotron Radiation Facility. https://doi.org/10.15151/ESRF-ES-644167190 (2025).

80. Ecker, W. et al. Nanoscale evolution of stress concentrations and crack morphology in multilayered CrN coating during indentation: Experiment and simulation. *Mater. Des.* **188**, 108478 (2020).

81. Keckes, J. et al. X-ray nanodiffraction reveals strain and microstructure evolution in nanocrystalline thin films. *Scr. Mater.* **67**, 748–751 (2012).

82. Feigin, L. A. & Svergun, D. I. *Structure Analysis by Small-Angle X-Ray and Neutron Scattering*. https://doi.org/10.1007/978-1-4757-6624-0 (Springer New York, N, 1987).

83. Zeilinger, A. et al. In-situ observation of cross-sectional microstructural changes and stress distributions in fracturing TiN thin film during nanoindentation. *Sci. Rep.* **6**, 22670 (2016).

84. Tian, F., Károly, L., Shen, J. & Vitos, L. Calculating elastic constants in high-entropy alloys using the coherent potential approximation: Current issues and errors. *Comput. Mater. Sci.* **111**, 350–358 (2016).

85. Zener, Clarene Theory of the elasticity of polycrystals with viscous grain boundaries. *Phys. Rev.* **60**, 906–908 (1941).

86. Tvergaard, V. Material Failure by Void Growth to Coalescence. *Adv. Appl. Mech.* **27**, 83–151 (1990).

Acknowledgements

Author contributions

Conceptualization: M.M., M.A. Methodology: M.M., M.A., and J.T. Investigation: M.M., M.A., N.S., J.T., M.B., and M.R. Formal Analysis: N.S. and E.S. Resources: M.B., M.R., and A.H. Visualization: M.M., M.A., and N.S. Supervision: E.S., J.K., and D.K. Funding Acquisition: E.S., J.K., and D.K. Writing—original draft: M.M. and M.A, Writing—review & editing: M.M., M.A., A.H., N.S., J.T., M.B., M.R., E.S., J.K., and D.K.

Competing interests

The authors declare no competing interests.

Additional information

Supplementary information The online version contains supplementary material available at https://doi.org/10.1038/s43246-025-00752-z.

Correspondence and requests for materials should be addressed to Michael Meindlhumer or Markus Alfreider.

Peer review information : *Communications Materials* thanks the anonymous reviewers for their contribution to the peer review of this work. Primary Handling Editor: John Plummer.

Reprints and permissions information is available at http://www.nature.com/reprints

Publisher's note Springer Nature remains neutral with regard to jurisdictional claims in published maps and institutional affiliations.